Nuclear Instruments and Methods in Physics Research B 269 (2011) 1238–1242

Contents lists available at ScienceDirect

Nuclear Instruments and Methods in Physics Research B

journal homepage: www.elsevier.com/locate/nimb

Highly charged ion interactions with thin insulating films

J.M. Pomeroy [a,b,*], R.E. Lake [b], C.E. Sosolik [b]

[a] National Institute of Standards and Technology, Gaithersburg, MD 20899-8423, USA
[b] Dept. of Physics and Astronomy, Clemson University, Clemson, USA

ARTICLE INFO

Article history:
Received 12 October 2010
Received in revised form 29 October 2010
Available online 9 November 2010

Keywords:
Highly charged ions
WKB
Magnetic tunnel junction
Potential sputtering

ABSTRACT

The electrical conductance of magnetic tunnel junction (MTJ) devices whose ultra-thin aluminum oxide tunnel barriers were irradiated by highly charged ions (HCIs) increases linearly with the fluence of HCIs, while retaining a current–voltage relationship indicative of a tunnel junction. The slope of the MTJ conductance σ_c as a function of fluence varies with different tunnel barrier thicknesses d, levels of oxidation (stoichiometry) and charge state q. Since the MTJ conductance after HCI irradiation is due to tunneling, the increased conductance can result from thinning the barrier, reducing the effective tunnel barrier height φ, or both. Measurements of the current–voltage profile provide sufficient degrees of freedom to substantially constrain d and φ provided the reduction of the barrier remains within the assumptions of the commonly used WKB (Wentzel–Kramers–Brillouin) tunneling formalism. For the Xe^{32+} ions discussed here the perturbation of the tunnel barrier is much weaker than in our previously reported measurements of Xe^{44+} and application of WKB is still reasonable. This analysis reveals a trend of decreasing d while φ changes little.

Published by Elsevier B.V.

Introduction

Electronic excitations in solids, and even the interaction of swiftly moving charged particles, have been studied for the better part of a century, yet a robust description of the excitation and relaxation processes that occur when a highly charged ion (HCI) neutralizes on a solid surface remains the subject of scientific scrutiny. This is due in part to the unusually large energy densities, e.g. >20 keV/nm^3, that are created by the HCI neutralization energy, e.g., ≈52 keV per HCI for Xe^{44+}, and the extremely short time scales of the interaction. Not surprisingly, experimental studies (e.g., [1–4]) show the interaction is violent, with large numbers of secondary particles emitted along with X-rays and lower energy photons that can culminate in relatively large surface features, when one considers that a single atom created them. Collective work in this field has identified two important parameters that dominate the timescales of the interactions: (1) the HCI velocity, which (along with charge state) determines the extent of above-the-surface dynamics, and (2) the target's effective charge mobility, which controls the relaxation rate for the energy deposited by the HCI. Since the experimental methods utilized (either in real time or *post facto*), implicitly rely upon forcing as much of the interaction as possible to be at or above the surface, optimization of these surface methods has relied upon minimizing incident velocity and electronic mobility. Therefore, the materials extensively studied are mostly fluorides and oxides (graphite being a notable exception), which have essentially no mobility and are stable enough to facilitate *post facto* and *ex situ* examination of surface nanofeatures. These HCI created features, when studied with scanning probes, have typically been found to be either well formed "hillock" structures [3,4] of unknown composition, or caldera like structures [5–7] reminiscent of features created by swift, heavy ions [8] (SHI).

In an effort to access more and different information from the nanofeatures left by HCIs neutralizing on surfaces (or those from SHIs), we have developed a method of fabricating ultra-thin (≈1 nm) aluminum oxide films on a metal surface, irradiating them with HCIs to form nanofeatures, and then depositing another metal on top to form a magnetic tunnel junction (MTJ) device [9,10]. This approach has several notable advantages: (1) allows direct, electrical measurements of the HCI created nanofeatures, (2) encapsulates the nanofeatures to minimize effects due to chemical reaction with the environment or coarsening, thereby creating an archaeological record that can be re-measured many times with different techniques, (3) provides ensemble averages of a large, selectable number of features for each measurement, and (4) integrates over all modifications throughout the thickness of the tunnel barrier, i.e., the measurable interaction volume is not limited to the surface. For all the MTJs fabricated thus far, the electrical conductance of the irradiated MTJs is always seen to increase linearly with fluence, where the slope depends on the material properties of the aluminum oxide and the charge state of the HCI, e.g., see [11–13].

* Corresponding author at: National Institute of Standards and Technology, Gaithersburg, MD 20899-8423, USA. Tel.: +1 301 975 5508.
E-mail address: joshua.pomeroy@nist.gov (J.M. Pomeroy).

0168-583X/$ - see front matter Published by Elsevier B.V.
doi:10.1016/j.nimb.2010.11.006

In this paper, we present electrical measurements collected from HCI irradiated MTJs dosed using Xe^{32+} and Xe^{41+} that illustrate the basic behavior of this method, i.e., the linear increase in conductance with different slopes. The discussion is then focused on the samples irradiated with Xe^{32+} that have a relatively shallow slope corresponding to gentle modification of the tunnel barrier compared to higher charge states. Therefore, the thin barrier limit is avoided and the change in the electrical properties can be reasonably analyzed within a WKB (Wentzel–Kramers–Brillouin) tunneling formalism [14–16]. Using WKB, we extract the effective tunnel barrier parameters as a function of the HCI fluence, which show a systematic decrease in the tunnel barrier thickness while the tunnel barrier height remains essentially constant.

Experimental

The MTJ devices are fabricated and irradiated within a system of ultra-high vacuum (UHV) chambers connected with the National Institute of Standards and Technology (NIST) Electron Beam Ion Trap (EBIT), described in more detail elsewhere [17,18]. Thermally oxidized silicon substrates (approximately 1×2 cm) are loaded into vacuum and cleaned with an oxygen plasma. A lower electrode structure is deposited through a shadow mask that defines a longitudinal wire and portions of four lateral wires that identify four device locations per substrate. After the lower electrodes, a uniform (unmasked) ultra-thin layer of aluminum is deposited that provides a barrier both on top and on the sides of the lower electrodes. The aluminum is then exposed to an oxygen plasma for a predetermined time known to create a high quality tunnel junction. For each irradiation experiment, several (typically eight) substrates are prepared the day before and stored under UHV conditions overnight allowing the glassy aluminum oxide to sufficiently relax. Three of the four devices per substrate are then sequentially exposed to different fluences of HCIs, followed by immediate (typically <10 min) deposition of the encapsulating upper electrode structure that completes the electrical device. For the samples discussed here, the completed device structure is 2 Co+Ox/21 Co/1.1 Al+Ox[+HCIs]/10 Co/40 Cu/3 Au; thicknesses are in nm from bottom to top, "+Ox" indicates plasma oxidation, and "[+HCIs]" indicates different fluences of HCI irradiation for each device. The oxygen incorporation into the aluminum layer causes it to expand ≈45% so that the oxidized aluminum is estimated to be ≈1.5(1) nm [19].

Once completed, the substrates are removed from vacuum and measured in a four point configuration by applying constant current and measuring the voltage drop across the MTJ. For current–voltage (I–V) relationship, the current I is sequentially stepped and the voltage V measured at each point. For single point resistance measurements, the electrical resistance $R = V/I$ (conductance $g = I/V$) and for the I–V measurements $R = dV/dI$ ($g = dI/dV$). In both cases, the resistance (conductance) must be corrected for a geometric "negative resistance" artifact [20]. The cumulative uncertainties in conductance represent a 1 sigma propagation of uncertainties arising from uncertainties in the fluence, device size, negative resistance correction, and zero bias voltage offsets.

Results

MTJ electrical conductance g as a function of HCI fluence is shown in Fig. 1 for devices irradiated with $Xe^{32+}$and Xe^{41+}. Each datum represents a different MTJ device prepared according to the same process recipe but irradiated with a different fluence N. The data are then fit with a line to extract the slope of conductance σ_c, which corresponds to the average conductance of each HCI nanofeature. For the two charge states shown here, σ_c is a factor

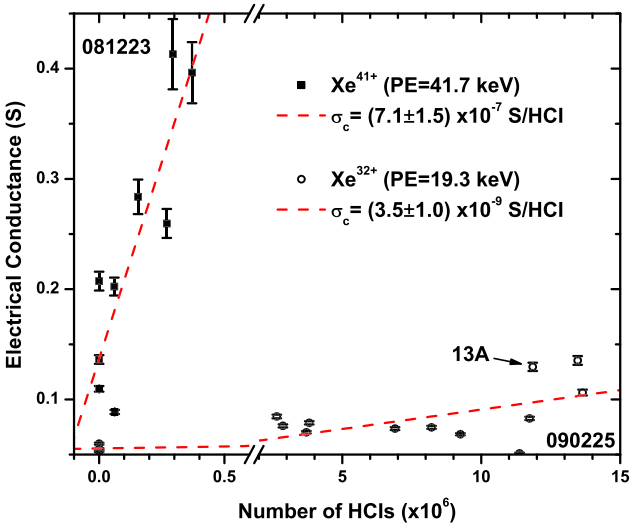

Fig. 1. The electrical conductance of tunnel junctions irradiated with HCIs increases linearly with the number of HCIs, shown for Xe^{41+} and Xe^{32+} on identically fabricated devices. The rate of conductance increase corresponds to an effective conductance produced per HCI σ_c, which depends on the initial conditions of the tunnel barrier and the charge state of the HCI. The datum indicated as "13A" corresponds to the data presented in Fig. 2.

of 200 different even though the HCI potential (neutralization) energies (PE) differ by only a factor of 2 (19.3 keV for Xe^{32+} and 41.7 keV for Xe^{41+}), the velocities by ≈15% and the estimated total (integrated through the ≈1.5 nm tunnel barrier) stopping power by <1% (6.82 keV for Xe^{32+} and 6.89 keV for Xe^{41+}). By way of comparison, a 10 nm^2 area of the unirradiated MTJ has a conductance of 5×10^{-11} S and each nanofeature produced from Xe^{44+} using this device recipe has a $\sigma_c \approx 5 \times 10^{-6}$ S. No evidence has been seen to suggest that the HCI affects the electrical performance of any portion of the device other than the tunnel barrier before coming to rest deep in the device substrate.

These measurements make clear that the nanofeatures produced by HCIs have a large electrical conductance. In order to assess whether the HCIs produce holes that penetrate through the barrier, particularly for the MTJ and charge combinations that result in σ_c values approaching a conductance quanta, we have performed measurements of the resistance vs. temperature (not shown, see [10]). For metallic through-holes, the resistance should increase with temperature. However, in all devices measured to date, the electrical resistance has always decreased with increasing temperature, characteristic of a tunnel junction. The HCI irradiated devices exhibit a resistance change that is very similar to (but slightly less than) the unirradiated control MTJs and both have a slope that implies the charge transport is occurring through tunneling [21].

To provide additional insight into the characteristics of the transport, the current vs. voltage relationship is measured and the first derivatives are calculated as is shown in Fig. 2. This example is taken from one of the most heavily dosed MTJs using Xe^{32+} and corresponds with device "13A" in Fig. 1. It exhibits a parabolic dependence typically seen in high quality tunnel junctions. (One should note that Joule heating would produce a curvature in the opposite direction.) Therefore, we conclude that in most of the cases (excepting some ultra-thin barriers irradiated with Xe^{44+}) the transport through the HCI produced nano-features is due to tunneling through a potential barrier.

Discussion

The data in Fig. 2 can be fit using an expression for the tunnel current density J based on the WKB approximation assuming the

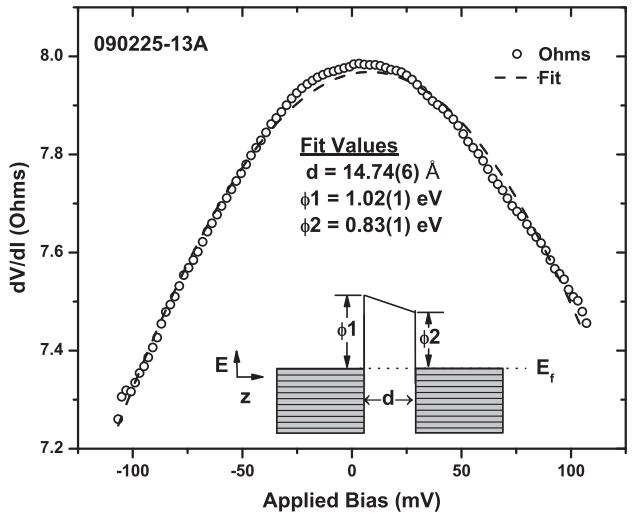

Fig. 2. Resistance vs. voltage data is shown in circles for device "13A" as shown in Fig. 1 that was irradiated with Xe^{32+}. This profile is fit using a tunneling formula based on the WKB formalism that allows the effective barrier thickness d and potential energy heights φ_1 and φ_2. The inset cartoon illustrates the geometry of the model with the applied bias $V = 0$, gray regions indicate filled electronic states. These fit values are included and correspond as indicated in Fig. 3. Uncertainties are contained within the size of the symbols.

energy diagram shown as an inset in Fig. 2. This approximation gives J as a function of voltage [14–16]:

$$J = \frac{3e}{4\pi h d^2}\left(\phi_{12}(V)\exp\left[-Ad\sqrt{\phi_{12}(V)}\right] - (\phi_{12}(V)+eV)\right.$$
$$\left.\exp\left[-Ad\sqrt{(\phi_{12}(V)+eV)}\right]\right)$$
$$\phi_{12}(V) = \frac{1}{d}\int_0^d dx\sqrt{\phi_1 - \frac{x}{d}(\phi_1 - \phi_2 + eV)} \quad (1)$$

where e is the electron charge, h is Planck's constant, $A = \frac{4\pi\sqrt{2m}}{h} \approx 1.025\ \text{Å}^{-1}\ \text{eV}^{-1/2}$, m is the electron mass, d is the tunnel barrier thickness, and ϕ_1 and ϕ_2 are the forward and reverse potential barrier heights. By allowing an unequal forward and reverse barrier height $\phi_1$and ϕ_2, the model accounts for the asymmetry in the data and the effective barrier height for both forward and reverse bias can be extracted from the fit. As can be seen in the data, the parabolic shape is centered about a voltage that is greater than 0 and is not the same on either side of the center. Both of these are indicators that the tunnel barrier is asymmetric despite the composition of the intended device being . . .Co/Al+Ox/Co. . .. This asymmetry is also observed in the unirradiated devices, as can be seen in Fig. 3, and is interpreted as a perturbation to the Fermi energy in the underlying Co due to excess oxygen from the aluminum oxidation process.

As is shown in Fig. 2, the data is well fit using Eq. (1) and allows the effective tunneling parameters to be extracted. In previous work [9], we found that the WKB formalism could not be reasonably applied to tunneling measurements when the HCI nanofeatures severely modified the tunnel barrier, as was the case for Xe^{44+} irradiation. Further, the low device resistances compared to the much larger electrode resistances in those samples provided substantial technical challenge to applying a sufficient bias (100 mV) across the junction that would allow the cubic part of the current–voltage relationship to be adequately measured. To avoid effects that may arise due to variations in the density of states near the Fermi energy, we always collect data between ±100 mV. Since the Xe^{32+} data presented in Fig. 1 have a relatively small σ_c, the HCI conductance through these nano-features are still

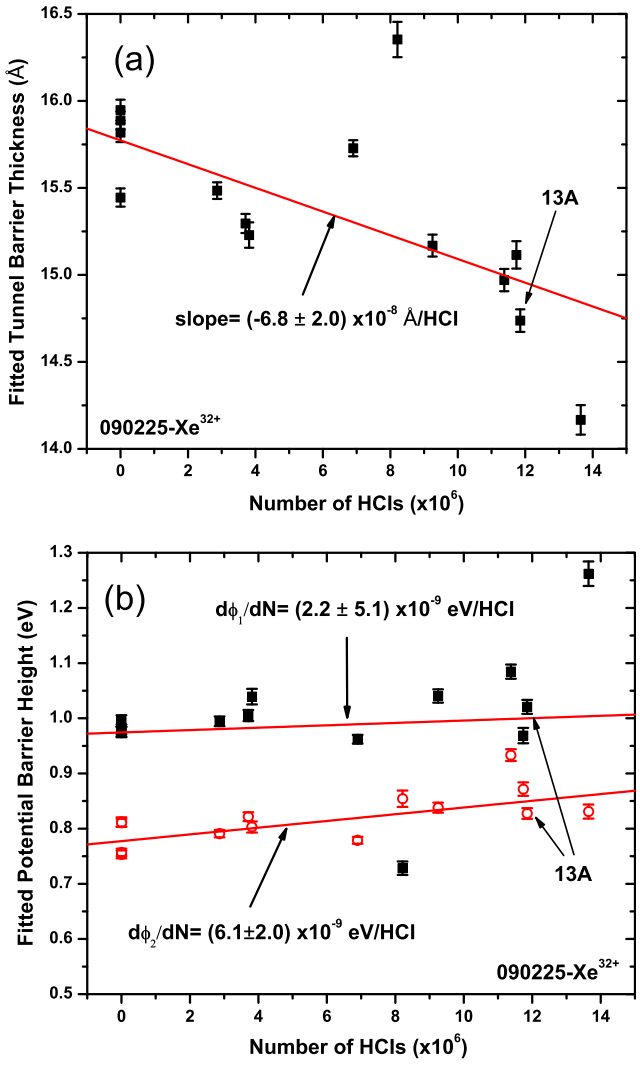

Fig. 3. (a) The fitted values for the tunnel barrier thickness d and (b) the potential energy heights φ_1 and φ_2 are shown for many identically fabricated devices irradiated with different fluences of Xe^{32+}. The tunnel barrier thickness is seen to systematically decrease, while the forward bias tunnel barrier φ_1 (filled squares) remains constant and the reverse bias tunnel barrier φ_2 (open circles) shows a subtle increase. These values represent a convolution of the unirradiated and irradiated portions, as discussed in the text. The uncertainties represent a 95% confidence interval for the fitted parameters.

within the range where the WKB formalism may be reasonably applied.

All the Xe^{32+} irradiated samples and the corresponding control devices shown in Fig. 1 have been fit in the same manner as the example shown in Fig. 2 to extract composite values of the tunnel barrier thickness and the forward and reverse bias barrier heights. These parameter values are shown in Fig. 3 as a function of the number of HCIs. The effective tunnel barrier thickness decreases by more than an Ångstrom over the range of the data. A linear fit establishes the rate of thinning and standard error, as shown, and indicates the observed change is statistically significant. Similarly, the forward bias barrier height φ_1 does not exhibit any change while the reverse bias barrier height φ_2 shows a small upward trend, as determined by comparison with the standard error.

In order to interpret these trends, we will use device "13A" (indicated in Figs. 3a and b) as an example. As is seen in Fig. 1, the zero bias conductance of 13A is 0.13 S after being irradiated with $\approx 1.19 \times 10^7$ Xe^{32+} ions compared to the unirradiated on-chip control "13D" which had a zero bias conductance of 0.053 S. The

addition of HCI produced nanofeatures with thinner barriers adds more current flow, so that the native barrier and HCI features can be considered as two independent channels. So when the current–voltage relationship is measured in Fig. 2, 41% of the current (0.053 S/0.13 S) is transmitted through the 9160 μm^2 of unirradiated tunnel barrier and the remaining 59% is transmitted through the dilute density of HCI nanofeatures. The fit parameters shown in Fig. 3 are therefore a convolution of the unirradiated tunnel junction and N HCI produced tunnel junctions, which we will assume are identical. In attempt to deconvolve these two contributions, we follow Brinkman et al. [14] by expanding Eq. (1) to third order and normalizing the conductance by the zero bias conductance so that:

$$G_{\mathrm{norm}}(V,d,\varphi_1,\varphi_2)=\frac{G(V)}{G(0)}=1-\left(\frac{Ad\Delta\varphi}{96\overline{\varphi}^{\frac{3}{2}}}\right)eV+\left(\frac{A^2d^2}{4608\overline{\varphi}}\right)(eV)^2 \quad (2)$$

where $\overline{\varphi}=\frac{(\varphi_1+\varphi_2)}{2}$, and $\Delta\varphi=(\varphi_2-\varphi_1)$. Taking the measurement as a sum of the two conductance contributions in parallel:

$$G^{13A}_{\mathrm{norm}}(V)=C^{13D}G^{13D}_{\mathrm{norm}}(V,d^{13D},\varphi_1^{13D},\varphi_2^{13D})+C^{\mathrm{HCl}}G^{\mathrm{HCl}}_{\mathrm{norm}}(V,d^{\mathrm{HCl}},\varphi_1^{13D},\varphi_2^{\mathrm{HCl}}) \quad (3)$$

where $G^{13A}_{\mathrm{norm}}(V)$ is the measurement of 13A, the C values are current weights 0.41 and 0.59, respectively (from above), $G^{13A}_{\mathrm{norm}}(V,\ldots)$ is the independent measurement of the control 13D that separately yields $d^{13D},\varphi_1^{13D},\varphi_2^{13D}$ (shown in Fig. 3) leaving $d^{\mathrm{HCl}},\varphi_1^{\mathrm{HCl}},\varphi_2^{\mathrm{HCl}}$ as unknowns. Since the normalization reduces the number of degrees of freedom to two, we eliminate, φ_1^{HCl} by setting it to φ_1^{13D}, since Fig. 3b indicates that φ_1 is unchanged by the HCI irradiation. Solving for the two remaining parameters, we find $d^{\mathrm{HCl}}=13.9$ Å and $\varphi_2^{\mathrm{HCl}}=0.84$ eV, compared with the convolved fit values (in Fig. 3) of $d=14.7$ Å and $\varphi_2=0.83$ eV. One might interpret the difference between $d^{\mathrm{HCl}}=13.9$ and $d^{13D}=15.44$ Å as the effective vertical size of the nano-feature, although no direct spatial information is available to support that conclusion. So, in the regime where both current paths (unirradiated barrier and HCI features) contribute non-negligible current, the initial barrier parameters are convolved with the HCI modified ones in a non-obvious way that provides an intermediate parameter value representative of neither. However, the deconvolution scheme used here as an illustration contains both differences and quotients of the data, amplifying the effects of measurement uncertainties so that most of the devices cannot be meaningfully deconvolved. So, while this analysis works in the case of chip 13, the d^{HCl} and φ_2^{HCl} parameter values have little statistical weight, but does reinforce the interpretation of an effective barrier thinning being the dominating effect.

Finally, we consider the physical implications of this data and the analysis. The HCI irradiation increases the electrical conductance of the devices in a dramatic fashion, which requires increases in the number of electronic states in the impact region of the insulator, manifest either as an effective thinning of the barrier or decrease in the barrier height. Since the conductance is dominated by the integral $\phi_{12}(V)$, the integral is reduced (more conductance) when more electronic states exist in the tunneling region. And since $\phi_{12}(V)$ represents the oxidized aluminum, these states likely indicate a local reduction in the oxygen (but does not exclude Al ablation). If the HCI irradiated aluminum oxide has a deficiency of oxygen, and the cobalt contains some excess oxygen, the higher Al–O bond energy will drive the oxygen back into the Al, restoring the symmetry of the tunnel barrier, consistent with the observed trend in Fig. 3b where ϕ_2 was becoming more like ϕ_1. Therefore, the systematic increase in conductance due to the decrease in the tunnel barrier thickness combined with the increasing symmetry of the tunnel barrier potential can be understood by HCI induced ablation and subsequent oxygen diffusion.

Conclusions

The integration of an MTJ structure with an HCI irradiated barrier provides a method of probing HCI induced nanostructures with electrical transport techniques. These measurements show that the nano-features are highly conducting compared to the properties of the previously insulating material, but still retain a quantum tunneling current–voltage characteristic. If the tunnel barrier is not too severely modified, as is the case for Xe^{32+}, the WKB approximation for the tunneling can be applied, revealing a systematic decrease in the effective tunnel barrier thickness while the potential barrier shape trends toward symmetric. To deconvolve the contributions from the unirradiated and irradiated portions of the sample, a simple two current model is implemented that suggests more likely values of the tunnel barrier thickness and effective barrier height for the HCI irradiated portion of the device. While the ability to use the WKB method is limited by small perturbations to the tunnel barrier, the ability to separate the two source of currents depends on high signal-to-noise, which is contradictory to using samples with weak perturbations. Application of this approach to data sets with greater dynamic range, smaller measurement uncertainties, or thicker barriers (where WKB can be used for larger perturbations) may offer a low uncertainty determination of the tunnel parameters.

References

[1] F. Aumayr, H. Winter, Potential Sputtering, Philosophical Transactions of the Royal Society of London 362 (2004) p. 77–102.
[2] T. Schenkel, A.V. Hamza, A.V. Barnes, D.H. Schneider, Interaction of slow, very highly charged ions with surfaces, Progress in Surface Science 61 (2–4) (1999) 23–84.
[3] S. Facsko, R. Heller, A.S. El-Said, W. Meissl, F. Aumayr, Surface nanostructures by single highly charged ions, Journal of Physics: Condensed Matter 21 (22) (2009) 9.
[4] F. Aumayr, A.S. El-Said, W. Meissl, Nano-sized surface modifications induced by the impact of slow highly charged ions – a first review, Nuclear Instruments and Methods in Physics Research Section B: Beam Interactions with Materials and Atoms 266 (12–13) (2008) 2729–2735.
[5] J.M. Pomeroy, A.C. Perrella, H. Grube, J.D. Gillaspy, Gold nanostructures created by highly charged ions, Physical Review B 75 (2007) 41409R.
[6] M. Tona, Y. Fujita, C. Yamada, S. Ohtani, Electronic interaction of individual slow highly charged ions with TiO2(110), Physical Review B 77 (15) (2008) 155427.
[7] M. Tona, H. Watanabe, S. Takahashi, N. Nakamura, N. Yoshiyasu, M. Sakurai, T. Terui, S. Mashiko, C. Yamada, S. Ohtani, Nano-crater formation on a Si(111)-(7 Ã— 7) surface by slow highly charged ion-impact, Surface Science 601 (3) (2007) 723.
[8] E.M. Bringa, K. Nordlund, J. Keinonen, Cratering-energy regimes: from linear collision cascades to heat spikes to macroscopic impacts, Physical Review B (Condensed Matter and Materials Physics) 64 (23) (2001). 235426/1–235426/12.
[9] J.M. Pomeroy, H. Grube, HCI potential energy sputtering measured with magnetic tunnel junctions, Nuclear Instruments and Methods in Physics Research Section B: Beam Interactions with Materials and Atoms 267 (4) (2009) p. 642–645.
[10] J.M. Pomeroy, H. Grube, A.C. Perrella, J.D. Gillaspy, Selectable resistance-area product by dilute highly charged ion irradiation, Applied Physics Letters 91 (7) (2007) 073506.
[11] J.M. Pomeroy, H. Grube, A.C. Perrella, J.D. Gillaspy, STM and transport measurements of highly charged ion modified materials, Nuclear Instruments \& Methods in Physics Research Section B: Beam Interactions with Materials and Atoms 258 (2007) 189.
[12] R.E. Lake, J.M. Pomeroy, C.E. Sosolik, Energy dissipation of highly charged ions on Al oxide films, Journal of Physics: Condensed Matter 22 (8) (2010) 084008.
[13] J.M. Pomeroy, H. Grube, Highly Charged Ion (HCI) Modified Tunnel Junctions, AIP Conference Proceeding Series 1099 (2009) 520.
[14] W.F. Brinkman, R.C. Dynes, J.M. Rowell, Tunneling Conductance of Asymmetrical Barriers, Journal of Applied Physics 41 (5) (1970) p. 1915–1921.
[15] C.K. Chow, Square-mean-root approximation for evaluating asymmetric tunneling characteristics, Journal of Applied Physics 36 (2) (1965) 559.
[16] J.G. Simmons, Electric tunnel effect between dissimilar electrodes separated by a thin insulating film, Journal of Applied Physics 34 (9) (1963) 2581.

[17] J.D. Gillaspy, J.M. Pomeroy, A.C. Perrella, H. Grube, The potential of highly charged ions: possible future applications, Journal of Physics: Conference Series 58 (2007) p. 451–456.
[18] J.M. Pomeroy, H. Grube, A.C. Perrella, Spatial and electronic characterization of nano-features created by highly charged ions, Radiation Effects and Defects in Solids 162 (7–8) (2007) 473–481.
[19] A.E.T. Kuiper, M.F. Gillies, V. Kottler, G.W.t. Hooft, J.G.M.v. Berkum, C.v.d. Marel, Y. Tamminga, J.H.M. Snijders, Plasma oxidation of thin aluminum layers for magnetic spin-tunnel junctions, Journal of Applied Physics 89 (3) (2001) 1965–1972.
[20] J.M. Pomeroy, H. Grube, Negative resistance errors in four-point measurements of tunnel junctions and other crossed-wire devices, Journal of Applied Physics 105 (9) (2009) 094503–094508.
[21] Y. Xu, D. Ephron, M.R. Beasley, Directed inelastic hopping of electrons through metal-insulator-metal tunnel junctions, Physical Review B 52 (4) (1995) 2843.